POLITECNICO DI TORINO
Repository ISTITUZIONALE

Real-time model-based estimation of injection rate in GDI systems

Original
Real-time model-based estimation of injection rate in GDI systems / Zhang, T., Ferrari, A., Vento, O.. - In: ENERGY. - ISSN 0360-5442. - 324:(2025). [10.1016/j.energy.2025.135756]

Availability:
This version is available at: 11583/2999895 since: 2025-05-06T11:25:11Z

Publisher:
Elsevier

Published
DOI:10.1016/j.energy.2025.135756

Terms of use:

This article is made available under terms and conditions as specified in the corresponding bibliographic description in the repository

Publisher copyright

(Article begins on next page)

19 November 2026

Energy 324 (2025) 135756



Contents lists available at ScienceDirect

Energy

journal homepage: www.elsevier.com/locate/energy





Real-time model-based estimation of injection rate in GDI systems

Tantan Zhang [a], Alessandro Ferrari [b], Oscar Vento [b,*]

[a] College of Mechanical and Vehicle Engineering, Hunan University, Changsha, China
[b] Energy Department, Politecnico di Torino, Corso Duca degli Abruzzi 24, Torino, 10129, Italy

ARTICLE INFO

Keywords:
GDI injector
High-pressure flow
Injected flowrate
Real-time estimation
Closed-loop control

ABSTRACT

A light-weight numerical model has been developed for real-time prediction of the injected flowrate in a Gasoline Direct Injection (GDI) injector. The simplified model consists of two one-dimensional constant-diameter pipes connected by means of a divergent tube: it receives, as input values, a pressure signal, measured upstream the injector, and a reconstructed needle lift trace, obtained through empirical correlations. Pressure waves propagation in the hydraulic circuit is efficiently simulated, and a satisfactory prediction of the nozzle pressure can be obtained. The simplified model has been extended to account for injector coking effects by incorporating a correction, based on measurements of the flowrate entering the injector. The model has been validated for a wide range of working conditions and the computational time is of approximately 30 ms, making it competitive for ECU implementation. The predicted injected flowrate can be used to obtain an estimation of the measured injected mass, with an error below 1 mg for medium and big injections schedules (injected quantity > 8 mg): this estimation can be employed as a feedback signal for developing a closed loop control of the the injected mass.

1. Introduction

One of the most significant sectors for energy consumption is transportation, and as the number of people owning automobiles increases globally, so does the energy required for them [1,2]. Through the use of innovative combustion and engine torque management techniques [3–5], by developing new injection systems layouts [6], by using renewable fuels [7] or e-fuels [8,9], and by analysing GDI spray performance [10,11], also in ultra-high-pressure conditions [12,13], researchers are working to lower the fuel consumption and pollution emissions of automobiles.

In this context, gasoline direct injection (GDI) engines represent the primary thermal power generators in hybrid electric vehicles, constituting a major propulsion system for automotive use [14]. These spark-ignited engines not only enable advanced combustion modes for improved efficiency [15], but also function as crucial testbeds for exploring e-fuels and biofuels, positioning themselves as primary candidates for alternative fuel use in automobiles [16].

The injection rate, representing the mass flowrate of fuel through the injector nozzle holes over time, is a critical variable connecting the GDI system with the combustion process. It plays a key role for developing numerical diagnostic models [17] and real-time control of combustion mode [18]. However, achieving continuous and direct measurement of this variable within the combustion chamber of a running engine is inherently unattainable, leading to the necessity of indirect measurement methods. Even under such circumstances, the real-time measurement of injected fuel mass during one hydraulic injection, or during double injections [19], proves to be challenging. Hence, the development of a lightweight model for on-board measurement of the injection rate time history holds great value.

Presently, few methods for estimating GDI injection rates are available. In Ref. [20], the injected flowrate has been directly reconstructed using correlations and complex equations taking into account injection parameters such as the energizing time, rail pressure and injector-downstream environment pressure, following a zero-dimensional approach, which provided satisfactory results in the considered measuring range. The approach presented in Ref. [21], based on an extensive dataset, utilizes artificial neural networks featuring two hidden layers to predict the injection rate. The inputs to the network comprise a limited set of scalar values, representing injection condition parameters and a specifically defined variable indicating the static injected flowrate under defined conditions. However, these inputs serve as control variables and lack comprehensive information concerning real-time injector internal hydrodynamics. Consequently, this methodology closely resembles the use of a multi-dimensional lookup table [22], although with the advantage of reducing the experimental time

* Corresponding author.
E-mail address: oscar.vento@polito.it (O. Vento).

https://doi.org/10.1016/j.energy.2025.135756
Received 16 January 2025; Received in revised form 20 March 2025; Accepted 21 March 2025
Available online 22 March 2025
0360-5442/© 2025 The Authors. Published by Elsevier Ltd. This is an open access article under the CC BY-NC-ND license (http://creativecommons.org/licenses/by-nc-nd/4.0/).

required.

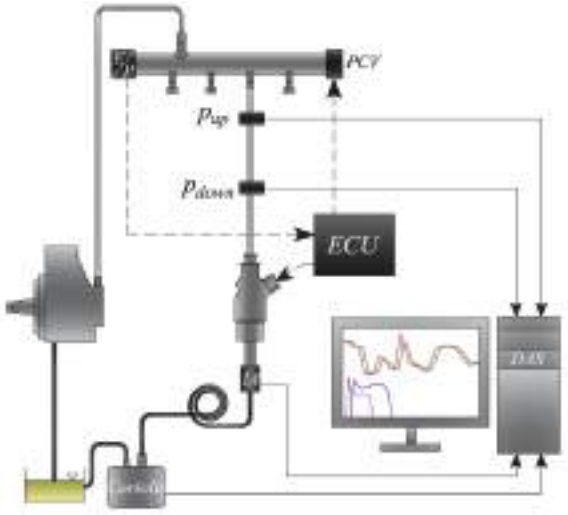
The related works of real-time injection rate measurement extend beyond GDI systems and encompasses other fuel-related injection systems. Given the similarity in application fields and the ballistic needle lift behavior shared by GDI and diesel common-rail injection systems [23], research in the latter may offer useful insights for developing the GDI injection rate estimation technique. Chung et al. [24] developed a 0D (zero-dimensional) model for near-steady-state characterization of injection rates in common-rail injection systems, with the model assuming a constant pressure input signal. This neglects the real-time hydrodynamic response of the system [25]. Satkoski et al. [26] introduced a simplified physics-based injection rate estimator for a diesel common-rail system with direct-acting injectors [27], effectively evaluating pulse-to-pulse interaction effects. However, this estimator employs a 0D model, which cannot adequately describe the pressure waves travelling forward and backward along the fuel line. Soriano et al. [28] and Perini et al. [29] developed phenomenological models for common-rail systems, where the injected mass per shot must be given as one input, posing an additional challenge for injection rate measurement. Fei et al. [30] estimated the injection rate of a common-rail system using an extended Kalman filter, and Wei et al. [31] developed a high-gain observer to estimate the ammonia injection rate of a diesel urea-SCR system. While these techniques cannot fully consider the characteristic waves along the fuel line, even though they can accurately measure slowly varied variables such as rail pressure time histories, it is questionable if these methods can accurately estimate the injection rate under different operating conditions between cycles. Williams et al. [32] developed two machine learning algorithms to estimate the injection rate of a diesel common-rail injection system with only one input signal of rail pressure. However, this sole input time history may generate considerable error in needle opening and closure instants under certain operating conditions, especially when residue pressure waves triggered by other injectors transmit into the rail. In Ref. [33], the injected flowrate of a piezoelectric injector has been predicted utilizing an artificial neural network algorithm, receiving as input four different quantities: the injection pressure, the injector-downstream environment pressure and temperature as well as the command signal duration. It should also be noted that machine-learning techniques can present a lack in the interpretability, since they are often based on a "black-box" approach, and they require a huge amount of data for a proper training [34].

In summary, while various techniques show promise for estimating GDI injection rates, they either lack essential hydrodynamic information for accurate measurement or require additional signals that are challenging to be measured during real working. Thus, there is margin to develop an injection rate estimation technique that is lightweight in computational load and capable of effectively estimating injection rates with sufficient physical information.

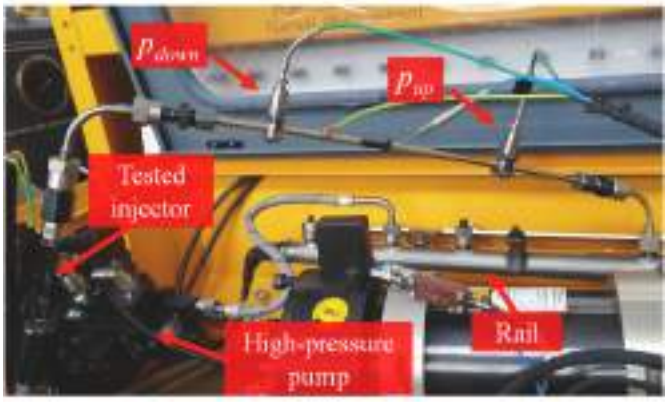
In this work, a fast-running 1D model has been developed for a GDI injector. From the analysis of a previously-validated complete 1D numerical diagnostic tool, a reduced version has been obtained by considering a simplified hydraulic circuit that is capable of reproducing the most relevant dynamic events occurring during an injection. Correlations to obtain a prediction of the needle lift trace are obtained, based on the nominal rail pressure value and the energizing time. The needle lift trace, together with a pressure signal measured in the hydraulic circuit, represents the input datum of the simplified numerical model, which is capable of providing an estimation of the injected flowratefor control purposes. The possible presence of coking deposits, which reduces the injected flowrate, is taken into account by the fast-running model by analyzing the flowrate entering the injector, obtained from a measured pressure signal along the rail-to-injector pipe.

2. Experimental facilities

Tests were conducted using a Rabotti TEC201 Evolution test bench.



(a) Schematic representation.



(b) Picture of the layout.

Fig. 1. – Experimental apparatus.

It is equipped with an electric motor, which allows speed control up to 4000 rpm. It also features a thermal regulation system for the tank and a low-pressure feed circuit that supplies pressurized oil to the high-pressure pump within a 0–40 bar range. The fuel injection system comprises the high-pressure pump, the rail, and various measurement devices such as pressure and temperature sensors, a Coriolis flowmeter, and an Injection Analyzer. The control signals for the injector and the rail/pump pressure control devices, specifically the pressure control valve (PCV) and the fuel metering valve (FMV), are generated by a custom-developed control unit. The rail pressure can be controlled in the 50–2500 bar range; in particular, the pressure control strategy monitors the average value over an injection cycle, therefore, the larger is the injection, the higher is the pressure at the beginning of the injection, to compensate the more pronounced pressure drop due to large energizing time (*ET*) values. This flexible test bench allows the management of injection pressure, the number of injections, the *ET* of each shot, the injection frequency, and the configuration of the injector current profile (including voltage, current levels, and the duration of each phase of the driving command), being suitable for both GDI systems and common-rail ones. The employed calibration fluid is the ISO 4113.

The experimental setup is schematically illustrated in Fig. 1a, and a picture is reported in Fig. 1b. A high-pressure rotary pump supplies fuel to the rail connected to the injector through an 840 mm long pipe with

Table 1
Features of devices constituting the experimental layout.

Device	Features
Pressure sensors	FSO = 500 bar; accuracy = ±1.25 bar
Injection Analyzer	Accuracy≤±0.1 mg/shot
Coriolis flowmeter	Measuring range = 0.1 ÷ 30 kg/h; Accuracy≤ ±0.1 %
Rail-to-injector pipe	Length = 840 mm; internal diameter = 1.9 mm

an internal diameter of 1.9 mm. Two piezoresistive pressure sensors are installed along this pipe: the upstream sensor (p_{up}) is situated 320 mm from the rail, while the downstream sensor (p_{down}) is located 200 mm downstream from p_{up}, closer to the injector.

The Injection Analyzer, a Bosch-method-based flowmeter (denoted as "IA" in Fig. 1a), measures the injected flow rate. The pressure signal is captured downstream of the injector tip, and the injected fuel travels through an 11-m-long pipe to prevent pressure wave reflections that could interfere with the injection process. A Coriolis flowmeter (SITRANS FC MASS2100 manufactured by Siemens), installed downstream of this pipe, is employed to measure the average flow rate.

Some features of the main devices of the experimental layout are reported in Table 1.

A scheme of the GDI injector, manufactured by Bosch and featuring 6 holes with a diameter of 220 μm, is represented in Fig. 2. In particular, a cross-section view of the injector is shown in Fig. 2a. The injector is normally closed, because the spring preload and the fuel pressure create a closure force, as reported in Fig. 2b. When the current signal activates the injector, a magnetic force generated by the solenoid pushes the needle upward, thereby initiating the injection process as illustrated in Fig. 2c. It is evident that, throughout the majority of the *ET* range, the injector operates under non-ballistic conditions.

When the current signal is turned off, the magnetic force ceases, causing the needle to complete its downstroke to close nozzle holes, thereby ending the injection. Due to the lack of a pilot stage, the GDI injector functions similarly to a fast two-way electro-valve with one inlet and one outlet port.

3. Injector numerical diagnostic model – validation and results

A detailed 1D numerical model of the injector, along with its feed pipe, has been created and validated in Ref. [35] using extensive experimental data from single injections at various nominal rail pressures (p_{nom}) ranging from 80 to 150 bar, while the energizing time has been varied from 270 μs to 5000 μs, covering most of the working conditions of actual engines for passenger cars featuring a GDI system. In fact, the selected range of working conditions in terms of p_{nom} and *ET* values includes the 1–85 mg range of injected mass. This diagnostic tool captures the essential elements of the high-pressure hydraulic circuit, the electromagnetic driving circuit, and the mechanical components. Fig. 3 presents a schematic of the injector numerical model. The circuit consists mainly of 0D chambers connected by 1D pipes. For boundary conditions, the pressure signal nearest the rail (p_{up}), as well as the current (I) and voltage (V) signals to the solenoid, were chosen to minimize inaccuracies in modeling the rail, pump, and the electronic control unit ECU. The fluid is assumed to be isothermal.

The pipe model uses the generalized Euler partial differential equations, solved with the Lax-Wendroff numerical method. The dynamic behaviour of the moving components is described by Newton's law in its ordinary differential form, using a mass-spring-damper approach. The forces in the numerical model include hydraulic, mechanical, and electromagnetic forces. Specifically, the electromagnetic force from the solenoid, F_E (referred to as "solenoid force (opening)" in Fig. 2c), acting on the needle is calculated as follows (sign minus is consistent with a

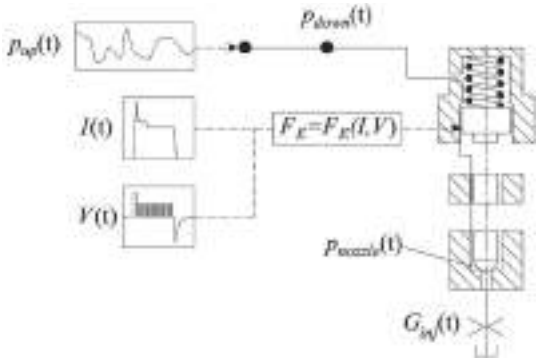


Fig. 3. Scheme of the numerical model of the GDI injector.

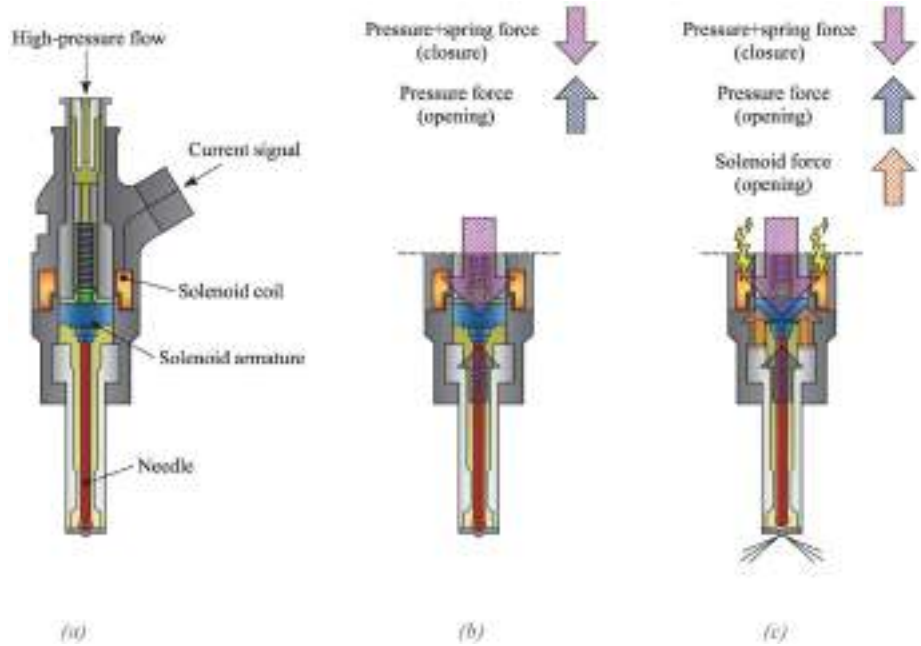


Fig. 2. – Scheme of the GDI injector.

Table 2
Main geometrical features of the tested injector.

Property	Value
Number of holes [−]	6
Nozzle hole diameter [mm]	0.22
Needle length [mm]	30.9
Needle ball diameter [mm]	2.7
Armature diameter (d_a) [mm]	10
Annular passage length (L_c) [mm]	4.45
Armature radial distance (δ_r) [mm]	0.12

force acting along the opening direction of the needle):

$$F_E = -\frac{1}{2}\Phi^2\frac{d\Re}{dx} \tag{1}$$

where $\frac{d\Re}{dx}$ represents the change in circuit reluctance, denoted as $\Re$, relative to the needle lift, and Φ represents the magnetic flux, which can be expressed as:

$$\Phi = \frac{1}{S}\int_0^t [V(t) - RI(t)]dt \tag{2}$$

The variables V and I denote the applied voltage and current to the injector solenoid, while R and S represent the measured resistance and the number of windings in the solenoid. Therefore, based on Eq. (2), by knowing the measured voltage and current applied to the injector solenoid, the magnetic flux can be determined, and, from Eq. (1), the electromagnetic force is calculated for each ET and it is applied as an opening force to the needle, as represented in Fig. 3.

As the needle moves, a viscous force arises between the armature and the injector body due to a thin boundary layer. Flow in this narrow annular passage is laminar and conforms to Poiseuille's law. Consequently, the viscous friction force acting on the armature can be quantified as [36]:

$$F_{vis} = \frac{\eta \bullet L_c \bullet v \bullet \pi \cdot d_a}{\delta_r} \tag{3}$$

where d_a is the armature diameter, L_c is the length of the annular passage, δ_r is the radial distance between the armature and the injector holder, η is the flow dynamic viscosity, and v is the velocity of the needle. This force is taken into account while solving the mechanical equilibrium of the needle.

The key geometrical features of the GDI injector investigated and implemented in the numerical model are detailed in Table 2.

The model validation consisted of the comparison between both the numerical injected flow rate (G_{inj}) and the numerical pressure time history p_{down} with the corresponding experimental data. Additionally, numerical injector characteristic curves for different rail pressure levels within the specified range were generated and compared with the experimental curves.

Fig. 4 presents the comparisons of p_{down} and G_{inj} time histories for single injections under various working conditions. In these plots, symbols represent the experimental data, while lines represent the numerical results. The comparisons indicate that the numerical results align very closely with the experimental data across all tested conditions, demonstrating the model accuracy and reliability. The RMSPE (root mean square prediction error) for the p_{down} pressure signal is below 3.8 bar for all the working condition, while the RMSPE for the G_{inj} prediction is always below 0.42 g/s.

Since the forces balance on the needle strongly depends on the pressure in the hydraulic circuit (cf. Fig. 2), the ET value above which the injector behaviour becomes non-ballistic (i.e., the first ET values in

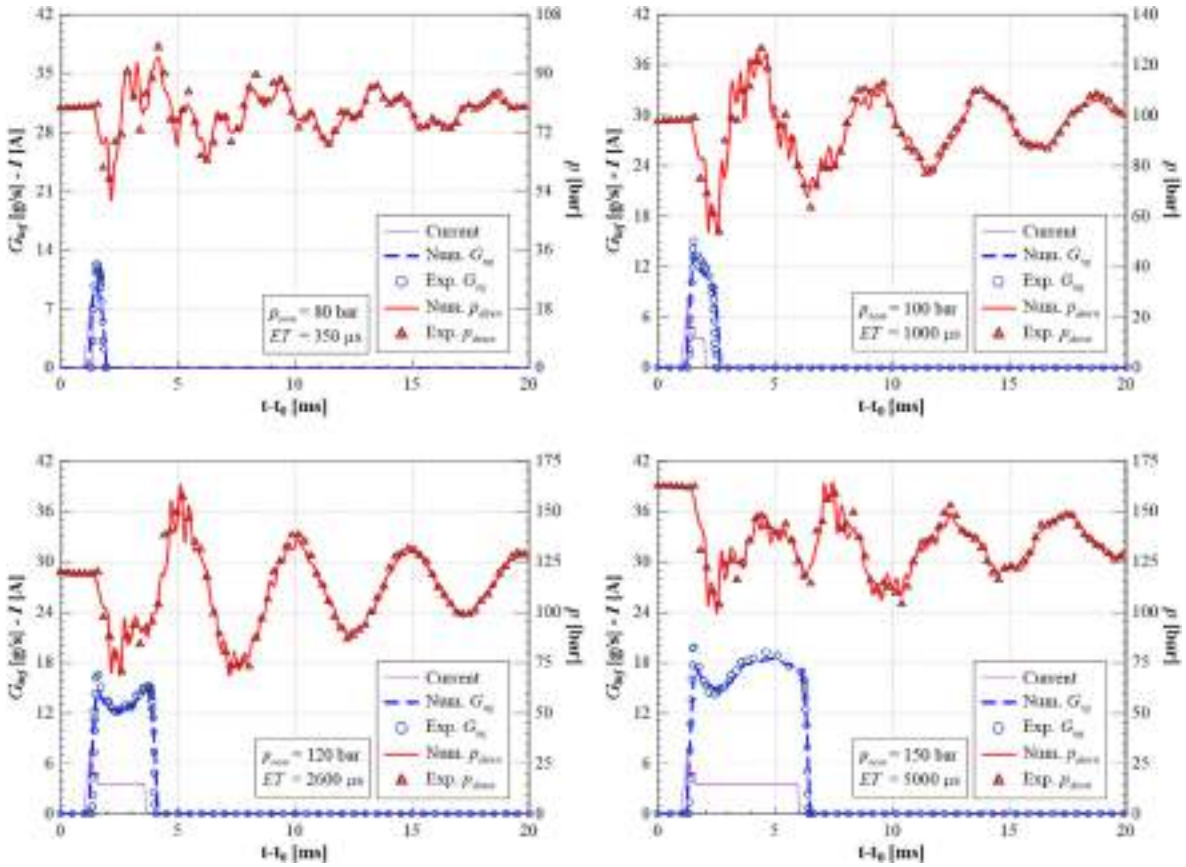


Fig. 4. Comparison of the numerical and the experimental results for single injections.

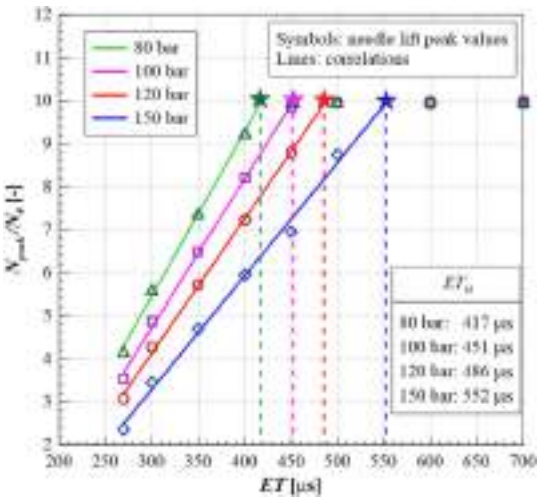


Fig. 5. Needle lift peak values in the ballistic working region of the injector.

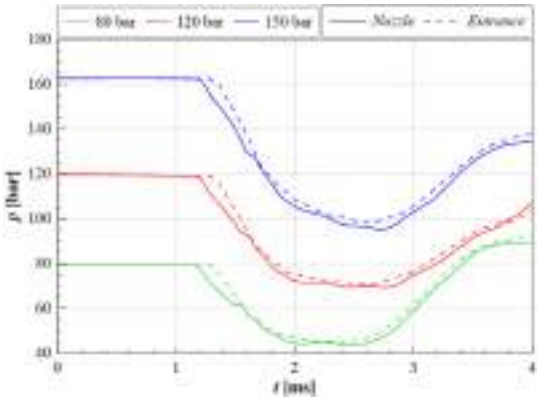


Fig. 6. – Comparison between the numerical pressure traces at the injector nozzle and at the injector entrance.

correspondence of which the needle reaches its upper stroke end, labeled as ET_{bl}) changes with the injection pressure. Fig. 5 shows the numerical normalized maximum needle lift peak values featured by the needle for different *ETs*, for the considered pressure levels. In particular, symbols refer to the results given by the numerical tool, while lines represent linear correlations of the data. Finally, the star symbols represent the point in correspondence at which each linear correlation has reached the upstroke-end needle lift value (corresponding to $ET = ET_{bl}$). As can be inferred from Fig. 5, the higher is the pressure, the higher is the *ET* value for which the needle reaches the upper-stroke end. This can be easily understood because the pressure closure force continuously acts on the needle, opposing its movement. This is also why the injected mass, for the ballistic-*ET* range, decreases as the pressure increases (this behavior is different from that of a solenoid diesel injector, due to the presence of the pilot stage in the latter case).

From the analysis of the 1D numerical model it can be noticed that the pressure time history inside the injector circuit does not change appreciably. This can be ascribed to the simple injector internal architecture. Fig. 6 reports, for different working conditions, the numerical pressure time histories measured inside the nozzle (solid line) and at the entrance of the injector (dashed line). It can be seen that corresponding solid- and dashed-lines pressure signals are affected almost by the same oscillations, and the main difference is a shift because the considered pressure time histories refer to different spatial locations: the finite velocity at which pressure waves travel in the hydraulic circuit, i.e., the speed of sound, justifies the time shift between the oscillations affecting the pressure time histories.

Such a wave propagation occurring through the injector and its feeding pipe can be efficiently modeled by considering a simplified model consisting of a 1D pipe (its features will be illustrated in the following section), and by monitoring a pressure time history along the rail-to-injector pipe, that is closely linked to the nozzle pressure (the latter is not usually measured when the injector is installed on the engine). In this way, a satisfactory prediction of the pressure time history inside the nozzle can be obtained, that is the one that influences the injected flowrate, without considering any moving part or electromagnetic component.

4. Simplified numerical model for control purposes

A light-weight numerical model, as illustrated in Fig. 7, has been developed to facilitate real-time monitoring of the injected flowrate, which is a critical input for the control system managing combustion within the cylinder. This model receives the experimental p_{down} pressure trace as boundary condition, along with the values of the nominal pressure value (p_{nom}) and *ET*.

A Simplified hydrodynamic model

In Fig. 7, the simplified injector hydrodynamic model is depicted, comprising a 1D pipe with a final restrictor that is opened following the needle lift trace. The 1D pipe, inclusive of a divergent section, simulates the pipe-like high-pressure circuit, delineated from the pressure sensor measuring p_{down} to the injector nozzle. No moving parts, such as the needle and the armature, are considered, therefore no equations of mechanics for mobile elements must be taken into account and solved. Similarly, no electromagnetic forces must be considered. The restrictor is employed to model the flow area constrained by the needle-seat passage and the nozzle: the needle-seat passage and the pressure drop across the nozzle holes predominantly restrict the flow during a hydraulic injection according to the needle lift [37]. Finally, a constant pressure reservoir downstream of the restrictor represents the outlet environment in the hydraulic test rig. Table 3 reports the main features of the simplified GDI 1D model. As an alternative to p_{down}, the p_{up} experimental signal could be provided as boundary condition: in this case, the pipe length L_1 should be increased by 200 mm, that is the distance between p_{down} and p_{up} pressure sensors in the hydraulic circuit,

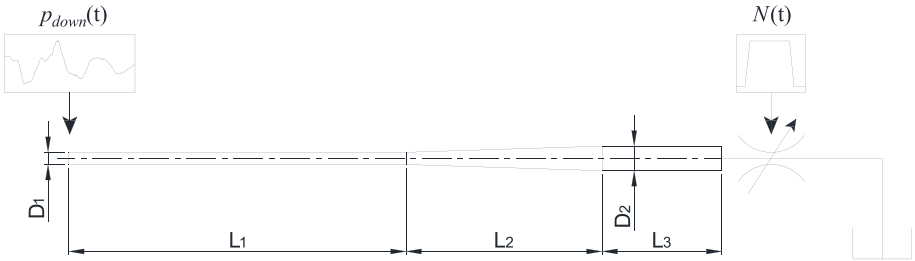


Fig. 7. – Schematic of the simplified GDI Injector.

Table 3
Features of the simplified GDI model.

Property	Value
Pipe length L_1 [mm]	290
Pipe length L_2 [mm]	120
Pipe length L_3 [mm]	60
Diameter D_1 [mm]	1.9
Diameter D_2 [mm]	4.5
Restrictor maximum diameter [mm]	0.523
Restrictor discharge coefficient C_d [−]	0.530

letting the simplified model to correctly predict the pressure waves propagation.

The hydrodynamic behavior of the 1D pipe is described by the following generalized Euler equations, implemented with a small number of computational nodes. These equations include continuity law and momentum balance, incorporating source terms for variation in flow area and wall friction:

$$\frac{\partial}{\partial t}\begin{bmatrix}\rho\\ \rho u\end{bmatrix}+\frac{\partial}{\partial x}\begin{bmatrix}\rho u\\ \rho u^2+p\end{bmatrix}=\begin{bmatrix}-\frac{\rho u}{A}\cdot\frac{dA}{dx}\\ -\frac{4\tau_w}{D}\end{bmatrix} \tag{4}$$

Independent variables x and t denote the spatial and temporal coordinates of the system, while ρ, u, p, D, and A represent the average cross-sectional density, velocity, pressure of the fuel along the pipe, internal diameter, and internal cross-section of the pipe, respectively. Additionally, τ_w stands for the 1D wall shear stress due to friction. In regions where flow area remains constant, dA/dx obviously becomes null.

The thermodynamic evolution is assumed to be isothermal and the fluid state equation simplifies to $\rho = \rho(p)$; this relationship can be accurately modeled with data conforming to the ISO 4113 standard.

Eq. (4) is presented in the form of quasi-linear hyperbolic partial differential equations. In this system, the low Mach number prevents the generation of shocks. Consequently, it can be diagonalized into a set of non-linear convection equations as follows [38]:

$$\frac{\partial \mathbf{W}}{\partial t}+\mathbf{\Lambda}\frac{\partial \mathbf{W}}{\partial x}=\mathbf{H} \tag{5}$$

where $\mathbf{\Lambda}$ is the diagonalized Jacobian matrix of the system. Introducing the sound speed definition, i.e. $a=\sqrt{dp/d\rho}$, $\mathbf{\Lambda}$ can be expressed as a function of eigenvalues λ_1 and λ_2:

$$\mathbf{\Lambda}=\begin{bmatrix}\lambda_1 & 0\\ 0 & \lambda_2\end{bmatrix}=\begin{bmatrix}u-a & 0\\ 0 & u+a\end{bmatrix} \tag{6}$$

The characteristic variables $\mathbf{W}$, presented in their differential form, are as follows:

$$\delta\mathbf{W}=\begin{bmatrix}\delta w_1\\ \delta w_2\end{bmatrix}=\begin{bmatrix}\delta\rho-(\rho/a)\delta u\\ \delta\rho+(\rho/a)\delta u\end{bmatrix} \tag{7}$$

The source term $\mathbf{H}$ is detailed as:

$$\mathbf{H}=\begin{bmatrix}h_1\\ h_2\end{bmatrix}=\begin{bmatrix}\frac{4\tau_w}{aD}-\rho u\cdot\frac{(u+a)}{a}\cdot\frac{dA}{Adx}\\ -\frac{4\tau_w}{aD}+\rho u\cdot\frac{(u-a)}{a}\cdot\frac{dA}{Adx}\end{bmatrix} \tag{8}$$

The wall shear stress is expressed as the sum of the Darcy-Weisbach friction shear stress and the unsteady friction shear stress of Kagawa type [39], with the detailed formulation available in Ref. [40]. The accuracy of injection rate measurement is strictly linked to the time step size. Given the ISO-4113 oil sound speed ranging from 1300 m/s to 1500 m/s across the operational conditions, employing a time step within the range of $12 \div 13$ μs and a space step of 1.81 cm represents the best threshold between accuracy of results and computational time, ensuring also the stability of the numerical scheme.

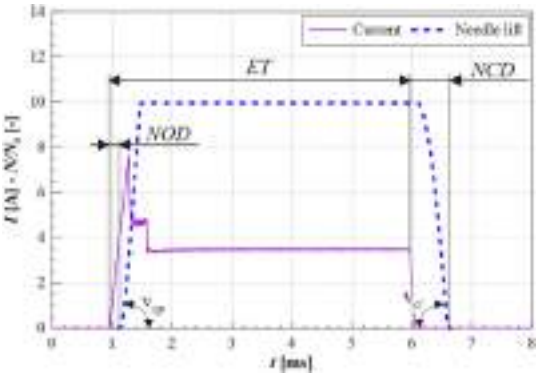


Fig. 8. – Needle lift trace and current signal to the solenoid.

The restrictor, located downstream from the pipe, is modeled by applying Torricelli's formula for quasi-steady-state flow, expressed as follows:

$$Q_{out}=C_d A_{nl}\sqrt{\frac{2|\Delta p|}{\rho_{mean}}} \tag{9}$$

where Q_{out} represents the volumetric flowrate at the nozzle outlet, C_d is the flow coefficient of the restriction, Δp is the pressure difference between the pressure of the final node at the downstream end of the pipe and the constant back pressure, and ρ_{mean} is approximated using the mean density value between values at the final node and in the back pressure reservoir. Finally, the restriction area A_{nl} is defined by the needle lift estimation, which is discussed in Section 4.B.

A finite-difference single-step Lax-Wendroff numerical scheme is employed to discretize the system of hyperbolic partial differential equations given by Eqs. (5)–(8) to reduce dissipation error [38], and the numerical scheme between instant t_n and t_{n+1} at the space coordinate j is expressed as follows:

$$w_{i,j}^{n+1}=\frac{1}{2}c_{i,j}^n\cdot\left(1+c_{i,j}^n\right)\cdot w_{i,j-1}^n+\left(1-\left(c_{i,j}^n\right)^2\right)\cdot w_{i,j}^n-\frac{1}{2}c_{i,j}^n\cdot\left(1-c_{i,j}^n\right)\cdot w_{i,j+1}^n+h_{i,j}^n \tag{10}$$

where $c_{\,i}$ denotes the Courant number, defined as $c_i=\lambda_i\bullet\Delta t/\Delta x$, with Δt and Δx representing the size of time and space steps of the computational mesh. Additionally, $i=1,2$ specifies the characteristic directions as described in Eqs. (5)–(8).

Unlike the centered scheme used in the inner domain, the boundary conditions are modeled using the CIR scheme for simplicity [38]. The overall scheme is explicit, non-conservative, and one-step, achieving second-order accuracy for interior nodes and first-order accuracy at the boundaries.

According to Von Neumann stability analysis, the scheme is stable if the Courant-Friedrichs-Lewy (CFL) condition is met. Consequently, the maximum Courant number is maintained close to 0.9 to ensure stability.

B Needle lift estimation

Fig. 8 represents the experimental current signal and the corresponding numerical needle lift trend given by the 1D diagnostic model for an injection with $p_{nom}=80$ bar and $ET=5000$ μs. As can be inferred, the needle starts to move up after a certain delay with respect to the current signal rise, that is the nozzle opening delay (*NOD* in Fig. 8); similarly, at the end of the current signal, the needle closes the nozzle after a certain delay with respect to the end of current signal, that is the nozzle closure delay (*NCD* in Fig. 8). The needle starts its upstream stroke when the neat opening force overcomes the closure one, i.e., the

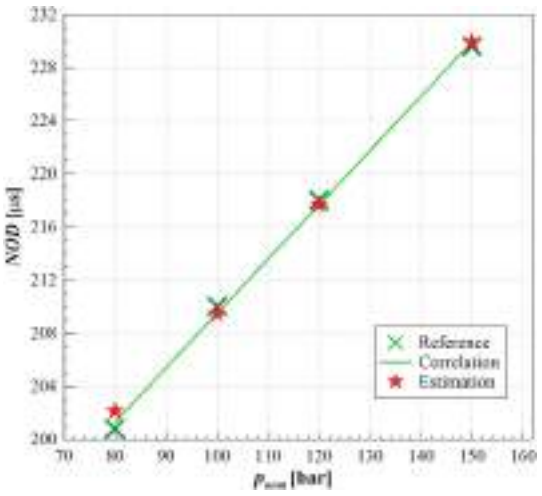


Fig. 9. – NOD dependency with respect to p_{nom}.

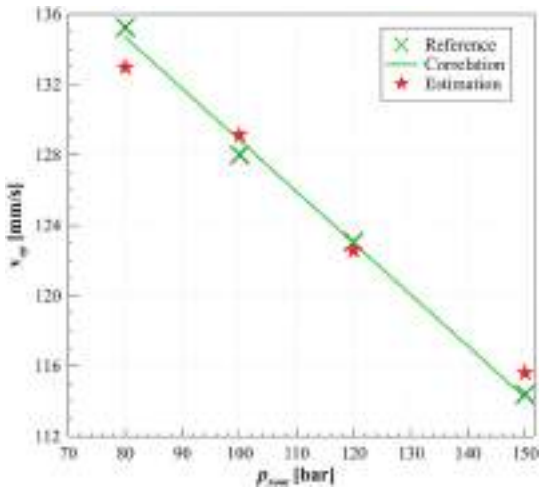


Fig. 10. – Needle opening velocity dependency with respect to p_{nom}.

electromagnetic force at the solenoid armature, together to the opening pressure force, generates a force greater than the closure pressure force and the spring force; on the contrary, the closure phase begins when the electromagnetic force goes below a certain value, for which the closure forces acting on the needle become predominant with respect to the opening one. The needle moves up and down with certain velocities, labeled as v_{op} and v_{cl} in Fig. 8, respectively. Since the simplified model requires the needle lift trace and this is not measured experimentally, the numerical results of the 1D diagnostic tool are used to determine a set of robust correlations to provide, for fixed values of p_{nom} and *ET*, all the parameters required to reconstruct the needle lift trace. The quality of the numerical needle lift traces taken as references were verified by means of the validation of the complete 1D diagnostic model (cf. Fig. 4).

Since the solenoid force is only a function of the electromagnetic characteristics of the injector (cf. Eq. (6)), it can be considered as constant for all the non-ballistic working conditions of the injector (this covers most of the cases for such injectors, due to the large *ET* values employed). Therefore, *NOD, NCD,* v_{op} and v_{cl} are mainly affected by the pressure regime inside the injector hydraulic circuit when the current starts to be supplied to the solenoid coil or when it stops. As far as the *NOD* is concerned, the higher the injection pressure, the greater is this delay, since the closure force against the needle movement is higher. The pressure control of the considered injection system can manage the average value of the pressure inside the rail, keeping it close to the nominal pressure value required by the ECU. Therefore, if an injection is characterized by a large value of *ET*, i.e., by a great value of injected mass, the pressure at the injection start is higher than that of a small injection, in order to compensate the more pronounced pressure drop featured by the hydraulic circuit during the bigger injection. This leads to the fact that *NOD* is also slightly affected by the *ET*, however, this dependency can be disregarded without introducing almost any inaccuracy in the needle trace prediction. Fig. 9 shows that the *NOD* values obtained from the experimental results, plotted as cross symbols and labeled as "Reference", are well correlated by means of a linear correlation. These experimental values can be obtained as the time interval between the start of the rise of the current and the start of the rise of the injected flowrate. The *NOD* values reported with the star symbols in Fig. 9 are those obtained by means of either extrapolation or interpolation of the experimental data. In particular, estimation results at 80 bar and 150 bar have been determined by performing an extrapolation of the correlation based on experimental data at 100 bar and 120 bar; the estimation of NOD at 100 bar and 120 bar are obtained by interpolating experimental data at 80 - 120 bar and 100-150 bar, respectively. This was made to prove the accuracy of the linear correlation, independently of the number of experimental points used to build it.

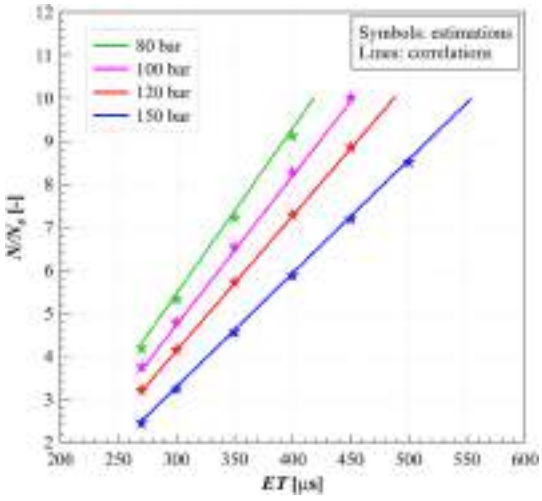


Fig. 11. – Needle lift peak value prediction for the ballistic-behaviour region.

Similar considerations can be made for v_{op}: this velocitycan be correlated to the rail nominal pressure level, as presented in Fig. 10. In this case, cross symbols refer to the mean needle velocity over the opening phase, obtained by the complete numerical model, labeled as "Reference", continuous line represents the correlation and star symbols refer to the estimated values of v_{op}, following the same approach applied for the *NOD*.

For completing the needle lift trace prediction, it is also necessary to know the needle lift maximum value. For a certain pressure level, if $ET \geq ET_{bl}$, the needle lift maximum value is equal to the needle stroke-end , while if $ET < ET_{bl}$, linear correlations can be used for the needle lift peak value prediction. In Fig. 11 the linear correlations of the normalized needle lift peak value (ballistic needle) vs *ET* are shown, together with the star symbols that represent the needle lift peak value prediction based on numerical data obtained from the complete numerical model.

As far as the descent phase of the needle lift, for an injection with $ET \leq ET_{bl}$ it is enough to know the closing velocity of the needle, i.e. v_{cl}, which can be provided by a correlation based on the nominal rail pressure level. This correlation is represented in Fig. 12, fitting the closure velocity values obtained by the complete numerical model and represented by the cross symbols, together with the estimated data given by the star symbols. Similarly to the opening velocity, the closure velocity is given by the average value of the derivative with respect to the time of the numerical needle lift trace along the needle closure phase.

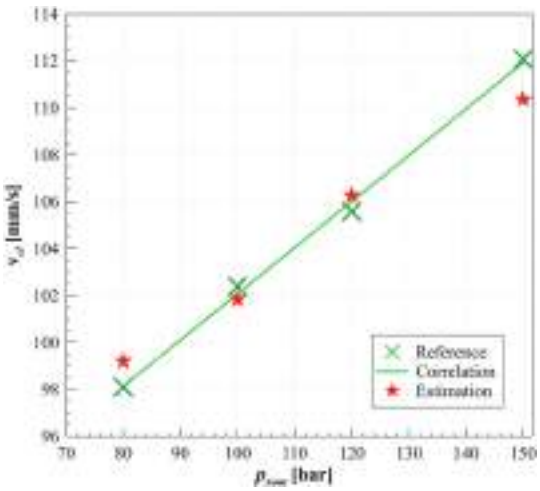


Fig. 12. – Needle closure velocity dependency with respect to p_{nom}.

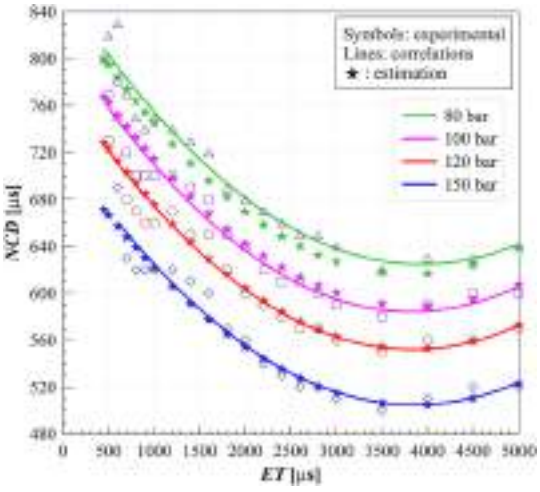


Fig. 13. – NCD dependency with respect to p_{nom} and ET.

If an injection has $ET > ET_{bl}$, it is necessary to know the nozzle closure delay (cf. Fig. 8), together with the needle closure velocity (cf. Fig. 12) in order to fully predict the needle lift. Fig. 13 reports the NCD values determined for different *ET*s at the considered nominal rail pressures (symbols), the second order polynomial correlations obtained for each pressure level (continuous line) and the estimations (star symbols) of the NCD values.

As can be seen from Fig. 13, the experimental nozzle closure delay (data in symbols) starts to sensibly reduce with the energizing time for injections characterized by ET>1600 μs, up to $ET \approx$ 3500 μs, and then tends again to increase. This decreasing-increasing trend can be explained by analyzing the pressure wave propagation across the hydraulic circuit. Furthermore, differences between the p_{up} and p_{down} pressure signals acquired along the rail-to-injector pipe, at a distance of 200 mm one from the other, can be interpreted based on the analysis of this waves propagation.

In the top part of Fig. 14, data are shown for the injected flow rate, p_{up}, p_{down} and p_{nozzle} pressure signals, and the current signal (*ET* starts at around 1 ms), corresponding to an injection with p_{nom}= 120 bar and ET= 5000 μs, whereas the lower part features a scaled schematic illustrating the propagation of pressure waves through the hydraulic circuit. Positioned on the left side of the lower graph, the schematic of the hydraulic circuit aligns spatial coordinates along the vertical axis.

At the opening of the injector nozzle and the subsequent rise in

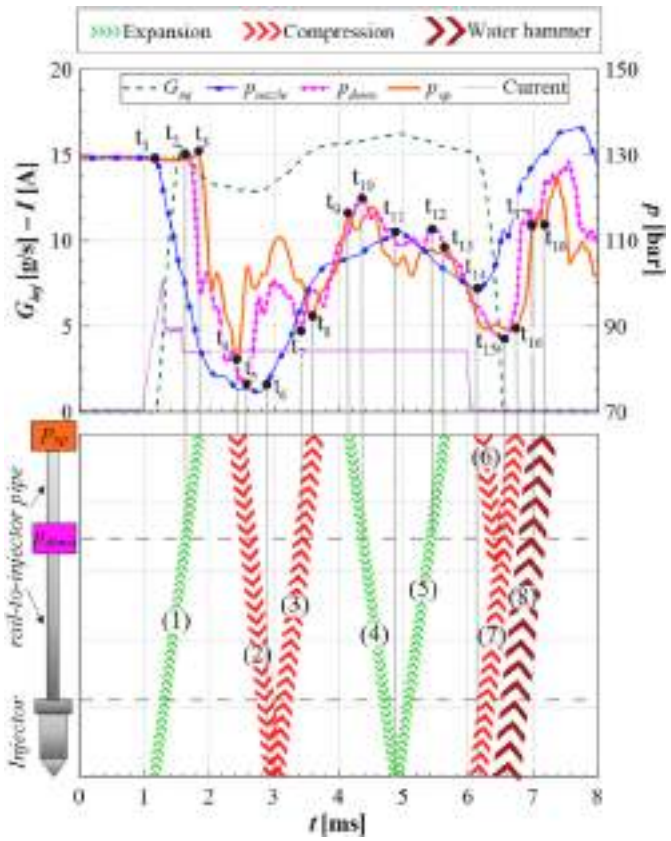


Fig. 14. – Pressure wave propagation in the hydraulic circuit (p_{nom} = 120 bar, ET=5000 μs).

injected flow rate, an initial expansion wave (labeled as (1)) arises in the nozzle (a pressure drop in p_{nozzle} can be recognized at time t_1) travelling from the injector to the rail throughout the hydraulic system. This propagation leads to a noticeable pressure drop first observed in the experimental signal p_{down} (at time t_2), followed by a delay before it affects p_{up} (at time t_3). Hence, starting from these time instants, the trajectory of expansion wave (1) can be depicted, as illustrated in the lower graph of Fig. 14, spanning the spatial positions associated with p_{up} and p_{down}.

The rail reflects the incoming expansion wave as a compression one (2); the p_{up} signal features a rise at t_4, earlier than that for p_{down}, which features the rise at t=t_5: this proves that this compression wave is travelling toward the injector. Wave (2) can be traced up to the nozzle, justifying the pressure rise in p_{nozzle} at t=t_6. When this wave reaches the injector tip, it is reflected keeping its nature, and the compression wave (3), travelling towards the rail, is observed; in fact, the p_{down} pressure features a rise at t=t_7 earlier than p_{up}, which increases at t=t_8. When this compression wave reaches the rail, it is reflected as an expansion wave (4), leading to a pressure reduction in p_{up} (t=t_9) and, subsequently, in p_{down} (t=t_{10}).

This expansion wave is extended up to the injector tip, giving a pressure reduction inside the nozzle at t=t_{11}. This wave is reflected as an expansion wave (5) moving toward the rail, as shown by the pressure drop occurring in p_{down} (t=t_{12}) and, after a certain time, in p_{up} (t=t_{13}). This wave is reflected at the rail as a compression wave (6); in the meanwhile, the closing phase of the needle begins, therefore, since the flowrate entering the injector is greater than G_{inj}, a compression wave (7) is triggered in the needle seat area (t=t_{14}) and travels towards the rail, as can be confirmed by the pressure rise in p_{down} (t=t_{15}), that is, in advance with respect to that in p_{up} (t=t_{16}). Finally, when the nozzle holes are closed (G_{inj} = 0), a water-hammer (8) arises in the nozzle, leading to a sharp pressure increment in p_{down} (t=t_{17}) and then in p_{up} (t=t_{18}).

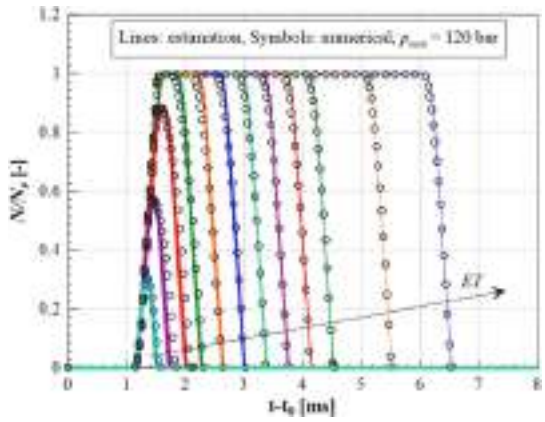


Fig. 15. Needle lift estimation for various energizing times (p_{nom} = 120 bar).

From this analysis it can be concluded that when compression waves (2) and (3) travel across the injector and reach the nozzle during the needle closure phase, leading to a pressure rise, the nozzle closure delay reduces (the closure force acting on the needle augments): pressure wave (2) enters the injector slighltly before t=3 ms in Fig. 14, then the phenomenon is evident for an injection with ET in the 1600÷1800 μs range. This also explain why experimental NCD in Fig. 13 does not show any remarkable decreasing trend for $ET \leq 1600$ μs (no other waves except the first expansion one travels across the injector-feeding pipe subsystem). On the other hand, if the expansion wave (4) has enough time to reach the injector ($t \approx 4.5$ ms, i.e. $ET \approx 3500$ μs), it, together with the reflected expansion wave (5), leads to a reduction in the pressure inside the injector: hence, the closure force diminishes and, when the current is switched-off, the needle requires a longer time to close the nozzle and to make the injection stop. Therefore, the pressure wave propagation, which only depends on the geometrical features of the hydraulic circuit (speed of sound dependency on pressure can be here neglected), affects the nozzle closure delay pattern, giving the reducing-increasing trend reported in Fig. 13. Based on this, even the closure velocity should be modified, for a fixed pressure, based on ET; however, it has been verified that the influence on the needle lift prediction of a constant closing velocity for all the ET values is marginal.

Fig. 15 reports the comparison between the needle lift traces obtained by means of the complete 1D numerical model and the estimated ones at various ETs (p_{nom} = 120 bar).

C. Effect of coking deposition on the equivalent orifice discharge coefficient

By means of the complete 1D diagnostic model of the GDI injector, the condition in which one or more nozzle holes result to be affected by coking deposits has been simulated by reducing the corresponding discharge coefficient. Due to the lack of experiments for these conditions, the numerical model pressure boundary condition has been substituted with a constant pressure value imposed on a fixed volume 0D chamber that models the rail of the injection system. When one or more nozzle hole features a reduced discharge coefficient, the needle lift trace does not change substantially, while the injected flowrate strongly diminishes. To account for this phenomenon in the simplified 1D-model, the discharge coefficient of the equivalent restrictor should be properly reduced. Six different obstruction levels have been considered in the complete 1D model, where the discharge coefficient has been directly modified from the nominal value, namely 0.9, to 0.2 for a progressively increasing number of injection holes, which ranges from 1 to 6 (as already mentioned, the nozzle has 6 injection holes). The results of these simulations, carried out with the complete 1D model and reported in Table 4, have been used to determine the values of the equivalent restrictor discharge coefficient of the simplified 1D numerical model and

Table 4
Discharge coefficients of the simplified model accounting for obstruction of nozzle holes.

Number of obstructed nozzle holes	Discharge coefficient (C_d) of the equivalent restrictor	Ratio with respect to the maximum value
0	0.530	100 %
1	0.502	94.74 %
2	0.465	87.72 %
3	0.418	78.95 %
4	0.363	64.42 %
5	0.288	54.39 %
6	0.195	36.84 %

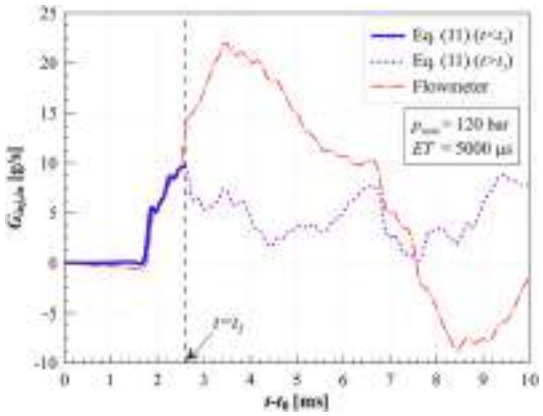


Fig. 16. Comparison between the flowrate obtained with the p_{down} signal and that given by a flowmeter.

the ratio, expressed as a percentage, of such a value of C_d to the maximum one (C_d = 0.530, cf. Table 3). It has been verified that the analysis reported in Table 4 is independent of the nominal rail pressure.

The flowrate entering the injector can be monitored as a feedback signal to properly reduce the discharge coefficient of the simplified-model restrictor in order to account for nozzle hole- obstructions. In fact, based on the analysis of the pressure waves propagation in the hydraulic circuit depicted in Fig. 14, the expansion wave (1) triggered by the injection start initially is the unique wave travelling in the rail-to-injector pipe. Up to the time instant t_5, when the compression wave (2) has reached the p_{down} sensor location, the instantaneous flow rate entering the injector, $G_{inj.in}$, can be worked out as [41]:

$$G_{inj.in}(t) = -A \int_0^{t_5} \frac{d(p_{down})}{a} \tag{11}$$

Equation (11) can be determined from the application of mass conservation and the momentum balance equation to the pressure wave front. Fig. 16 shows the flowrate obtained from Eq. (11)(continuous line from 0 to t_5, dashed line for $t > t_5$) compared to the injector-inlet flowrate measured by means of a high-pressure instantaneous flowmeter (dash-dot line), here used as a reference, from which it is evident the very good agreement for $t \leq t_5$.

When $ET > ET_{bl}$, the $G_{inj.in}$ peak value corresponding to $t = t_5$ in Fig. 16 keeps almost constant with respect to ET, and only changes with p_{nom}. Furthermore, this peak can diminish-, due to the presence of coking deposits that causes a reduction of the nozzle hole discharge coefficient (the continuity equation links the flowrate entering the injector to the injected one). When the injector is not aged and nozzle holes feature their maximum discharge coefficient, the peak of the injector inlet flowrate can be experimentally determined and stored in the ECU: the values for different pressures have been reported in Table 5.

The pressure sensor located in the proximity of the injector inlet can be used, based on Eq. (11), to monitor the entering flowrate. By computing the ratio between the actual entering flowrate peak value

Table 5
Entering flowrate peak values for different pressure levels.

p_{nom} [bar]	$G_{inj,in}$ peak value [g/s]
80	7.72
100	8.81
120	9.67
150	10.90

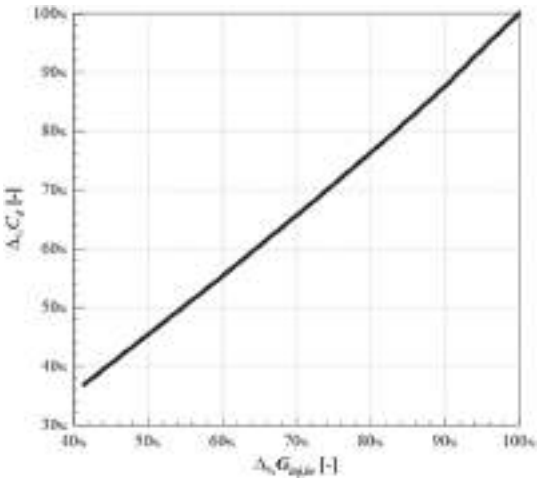


Fig. 17. Correlation between the variation of the entering flowrate peak value and the discharge coefficient.

with the stored one, it is possible to verify the obstruction level of the injector nozzle and therefore correct the discharge coefficient of the equivalent restrictor in the simplified model. The correlation reported in Fig. 17, gives the percentage scaling factor of the discharge coefficient ($\Delta_{\%}C_d$), referred to the maximum value for a new injector ($C_d = 0.530$), with respect to the ratio between the actual $G_{inj,in}$ peak value with respect to its maximum value (cf. Table 5), labeled as $\Delta_{\%}G_{inj,in}$. Such a correlation is almost linear and unique for all the pressure levels.

5. Results and discussion

The simplified numerical model is employed to estimate the measured injected flowrate. Fig. 18 shows the comparison between the experimental flowrates (symbols) and the numerical ones (lines) at different *ETs* for 80 bar, 100 bar, 120 bar and 150 bar. As can be inferred, the prediction results to be more accurate at high *ET* values rather than at short injections. In particular, when the injector is ballistic ($ET < ET_{bl}$) the prediction quality worsens. The reason can be ascribed to the fact that, in the simplified model, some of the dynamic effects, such as the interaction between the needle seat passages and the nozzle holes, are not modeled: this affects the pressure inside the sac, that is, the downstream pressure of the needle seat passage (in the presented model, this pressure coincides with the constant pressure of the Injection Analyzer discharge line where the injection occurs). Another dynamic effect, which is not modeled, regards the needle movement that modifies the sac volume during the injection, providing an unsteady contribution to the flowrate flowing through the needle seat passage. However, when $ET > ET_{bl}$ and the needle reaches its upstroke end, the needle seat passage variations with time play a minor role and the flowrate virtually

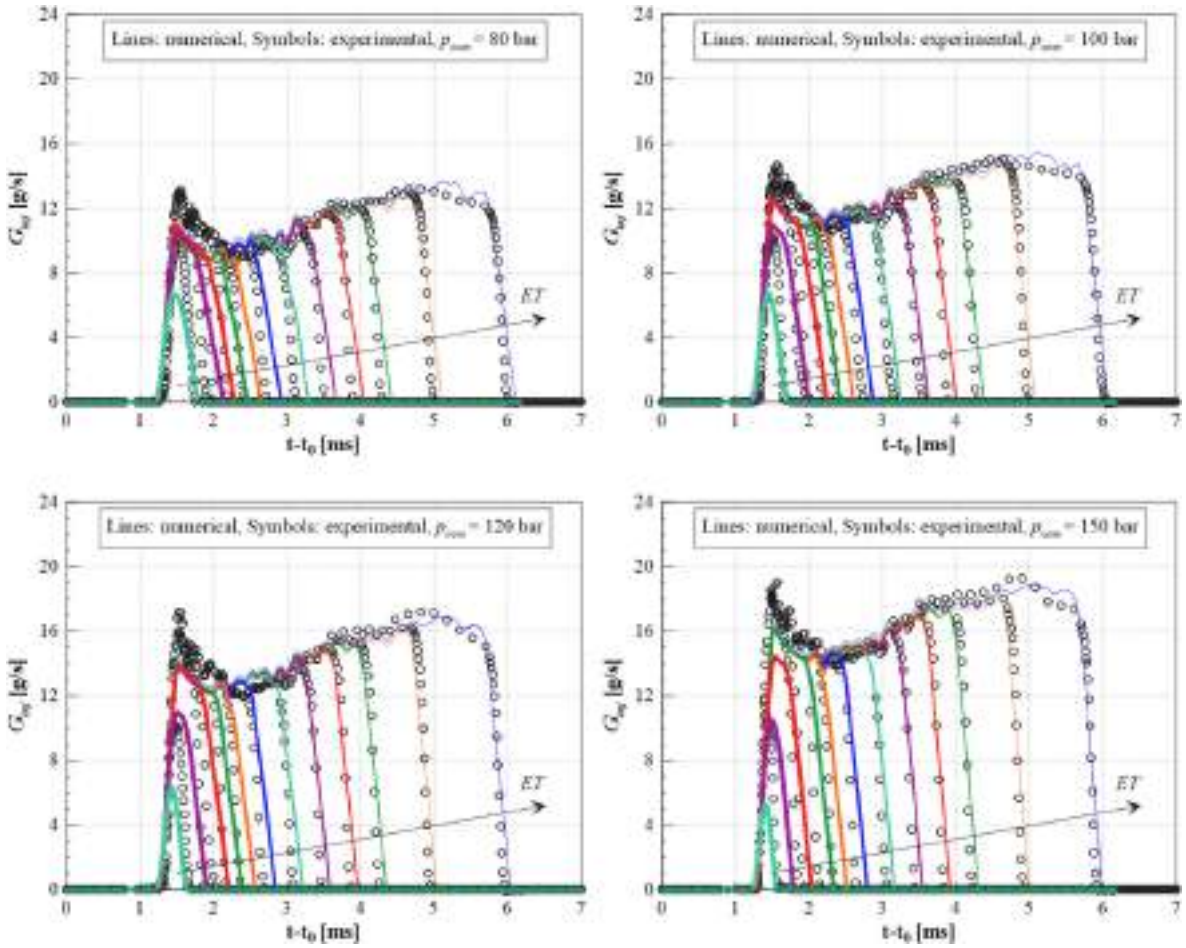


Fig. 18. – Comparison between the experimental flowrates and the ones provided by the simplified numerical model for different nominal pressures and ET values.

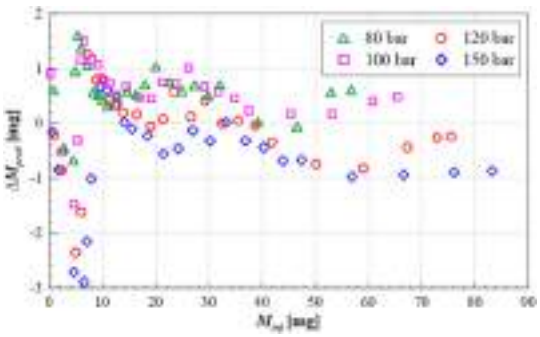


Fig. 19. Error in the prediction of the injected for different working conditions.

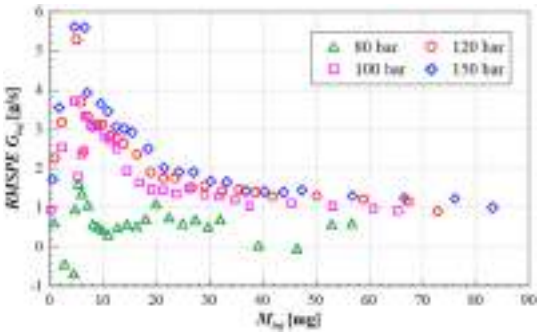


Fig. 20. – RMSPE of the injected flowrate prediction for different working conditions.

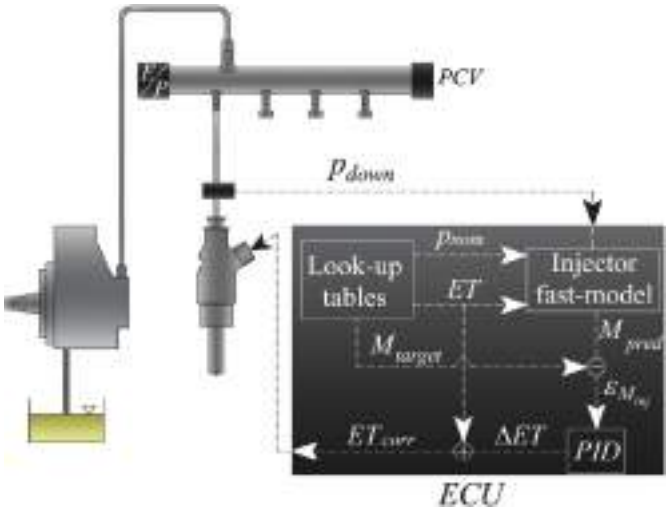


Fig. 21. Layout of a GDI injection system employing a closed loop control for the injected mass inaccuracy correction.

depends only on the pressure drop across the needle seat passage.

Fig. 19 reports, for the four considered nominal pressure levels, the difference between the predicted injected mass (M_{pred}), given by the integration of the numerical flowrate resulting from the simplified model, and the experimental one (M_{inj}), i.e. $\Delta M_{pred} = M_{pred} - M_{inj}$, plotted with respect to M_{inj}. As can be inferred, in line with Fig. 18, the injected mass prediction improves when ET augments and is at the moment not satisfactory for the injected quantities below 8 mg. If $M_{inj} >$ 8 mg, corresponding to most of the engine working conditions, the absolute error on the injected mass is lower than 1 mg. This satisfactory performance in terms of fuel quantity prediction can be used to set up a closed-loop control, where the energizing time provided to the injector can be corrected based on the error between the target mass value stored in the ECU and the prediction of the actual injected mass obtained from the simplified numerical model [42]. In Fig. 20, the RMSPE for the predicted flowrate is reported: in line with the results in Fig. 19, for injection schedules with small M_{inj}, the error in the prediction is larger than that for big injections.

A detail of a possible closed-loop control is presented in Fig. 21, where the difference $\varepsilon_{M_{inj}}$ between the target mass value (M_{target}) and the predicted one is the input value of a PID controller. The PID output value is the energizing time correction, namely ΔET, that, summed to the ET value provided by the ECU look-up table, gives the corrected energizing time value, ET_{corr}, acting on the injector in order to compensate the injected mass inaccuracy.

Numerical simulations have been performed by employing a workstation equipped with an Intel Core i7-4770 CPU (3.40 GHz) featuring 32 GB of RAM memory: the simplified model, implemented in MATLAB, provides a flowrate datum in around 0.033 s, while the complete numerical diagnostic model presented in Sect. 3 requires around 30 s: therefore, the simplified model shows promising potential for a ECU implementation for control and diagnostic purposes (even better performance can be obtained with a C++ implementation).

6. Conclusions

A light-weight numerical model has been developed for the injected flowrate real-time prediction of a GDI injector. This model is constituted by two 1D constant-diameter pipes connected by means of a divergent tube: at one extremity, the pressure signal measured along the rail-to-injector pipe is provided as boundary condition, while at the other extremity, a calibrated orifice features a restricted area, based on a reconstructed signal of the numerical needle lift trace. The latter is obtained by means of correlations to determine the NOD, the opening velocity, the needle lift peak value (for low ETs the injector is ballistic), the closure velocity and the NCD: these correlations have been obtained from a previously validated 1D complete injector model.

The complete numerical model has been used to analyze the injector behavior in the presence of coking deposits, by reducing the discharge coefficient of one or more nozzle holes: while the needle lift trace shows negligible modifications, the injected flowrate diminishes. To take this effect into account in the simplified model, a correlation has been determined to correct the discharge coefficient of the restrictor. Such a correlation is based on the measure of the flowrate entering the injector, which is obtained based on the pressure signal measured upstream of the injector.

The numerical flowrate provided by the simplified 1D model resulted in very good agreement with the experimental one for numerous working conditions (p_{nom} ranging from 80 to 150 bar, ET ranging from 270 μs to 5000 μs), featuring a competitive computational time for ECU implementation (this time was around - 30 ms). The injected mass can be obtained from the determined injected flowrate by means of time integration: this datum can be used to set up a control strategy that mitigates the injected mass inaccuracy. Such a prediction shows an inaccuracy below ±1 mg for measured injected quantities above 8 mg, while the injected mass prediction results to be unsatisfactory for $M_{inj}<$ 8 mg: the next objective is represented by a prediction improvement for the small injections.

CRediT authorship contribution statement

Tantan Zhang: Writing – review & editing, Writing – original draft, Validation, Software, Investigation, Funding acquisition, Formal analysis, Data curation. **Alessandro Ferrari:** Writing – review & editing, Writing – original draft, Supervision, Resources, Project administration, Methodology. **Oscar Vento:** Writing – review & editing, Writing – original draft, Visualization, Validation, Software, Methodology, Investigation, Formal analysis, Data curation, Conceptualization.

Declaration of competing interest

The authors declare the following financial interests/personal relationships which may be considered as potential competing interests: Tantan Zhang reports financial support was provided by National Natural Science Foundation of China (52406046). Tantan Zhang reports financial support was provided by Natural Science Foundation of Hunan Province (2024JJ6147). If there are other authors, they declare that they have no known competing financial interests or personal relationships that could have appeared to influence the work reported in this paper.

Acknowledgements

This work was financially supported by National Natural Science Foundation of China (52406046) and Natural Science Foundation of Hunan Province (2024JJ6147).

Nomenclature

0D	zero-dimensional
1D	one-dimensional
A	pipe cross-section area
a	speed of sound
C_d	discharge coefficient
c	Courant number
CFL	Courant-Friedrichs-Lewy
d, D	diameter, pipe diameter
ECU	electronic control unit
ET	energizing time
F	force
FMV	fuel metering valve
FSO	fuel scale output
G	mass flowrate
GDI	gasoline direct injection
$\mathbf{H}$	source term vector
I	current signal
IA	injection analyzer
L_c	length of the annular passage
L	pipe length of the simplified 1D model
M	mass
N	needle lift
NCD	nozzle closure delay
NOD	nozzle opening delay
p	flow pressure
PCV	pressure control valve
Q	volumetric flowrate
R	resistance
$RMSPE$	root mean square prediction error
$\Re$	reluctance
S	number of solenoid windings
t	time
u	flow velocity
V	voltage signal
v	needle velocity
$\mathbf{W}$	characteristic variables vector
x	spatial coordinate
$\Delta\%$	percentage scaling factor
ΔET	energizing time correction
ΔM_{pred}	difference between the reference injected mass and the predicted one
Δp	pressure difference
δ_r	radial distance between the armature and the injector holder
Φ	magnetic flux
Λ	Jacobian matrix
λ_1, λ_2	eigenvalues
η	flow dynamic viscosity
ρ	flow density
τ_w	wall shear stress

Subscritps

0	reference value
a	armature
bl	ballistic/non-ballistic treshold

cl	closure
corr	corrected
down	referring to the pressure sensor close to the injector
E	electromagnetic
inj	injected
inj,in	entering the injector
j	space coordinate
mean	average value
nom	nominal
n	time instant
nl	needle lift
nozzle	referring to injector nozzle
op	opening
out	nozzle outlet
peak	peak value
pred	prediction
target	target value
up	referring to the pressure sensor close to the rail
vis	viscous friction

Data availability

Data will be made available on request.

References

[1] Shah KJ, et al. Green transportation for sustainability: review of current barriers, strategies, and innovative technologies. J Clean Prod Dec. 2021;326:129392. https://doi.org/10.1016/j.jclepro.2021.129392.

[2] Zahoor A, Mehr F, Mao G, Yu Y, Sápi A. The carbon neutrality feasibility of worldwide and in China's transportation sector by E-car and renewable energy sources before 2060. J Energy Storage May 2023;61:106696. https://doi.org/10.1016/j.est.2023.106696.

[3] Finesso R, Marello O, Spessa E. Development of a pressure-based technique to control IMEP and MFB50 in a 3.0L diesel engine. Energy Proc Aug. 2018;148:424–30. https://doi.org/10.1016/j.egypro.2018.08.105.

[4] d'Ambrosio S, et al. Model-based control of torque and nitrogen oxide emissions in a euro VI 3.0 L diesel engine through rapid prototyping. Energies Feb. 2021;14(4):1107. https://doi.org/10.3390/en14041107.

[5] d'Ambrosio S, Mancarella A, Manelli A, Mittica A, Hardy G. Experimental analysis on the effects of multiple injection strategies on pollutant emissions, combustion noise, and fuel consumption in a premixed charge compression ignition engine. SAE Int J Engines Mar. 2021;14(5). https://doi.org/10.4271/03-14-05-0037. 03-14-05–0037.

[6] Jin Z, et al. Numerical-experimental optimization of the common-feeding injection system concept for application to light-duty commercial vehicles. J Energy Resour Technol Trans ASME 2021;143(12). https://doi.org/10.1115/1.4050133.

[7] Mancarella A, Marello O. Effect of coolant temperature on performance and emissions of a compression ignition engine running on conventional diesel and hydrotreated vegetable oil (HVO). Energies Dec. 2022;16(1):144. https://doi.org/10.3390/en16010144.

[8] Ueckerdt F, Bauer C, Dirnaichner A, Everall J, Sacchi R, Luderer G. Potential and risks of hydrogen-based e-fuels in climate change mitigation. Nat Clim Change May 2021;11(5):384–93. https://doi.org/10.1038/s41558-021-01032-7.

[9] Lindstad E, Lagemann B, Rialland A, Gamlem GM, Valland A. Reduction of maritime GHG emissions and the potential role of E-fuels. Transp Res D Transp Environ Dec. 2021;101:103075. https://doi.org/10.1016/j.trd.2021.103075.

[10] Ji M, Wu Z, Ferrari A, Fu L, Vento O. Experimental investigation on gasoline—water mixture fuel impingement preparation method and spray characteristics with high injection temperatures and pressures. Energies Aug. 2023;16(16):6026. https://doi.org/10.3390/en16166026.

[11] Huang W, Moon S, Gao Y, Wang J, Ozawa D, Matsumoto A. Hole number effect on spray dynamics of multi-hole diesel nozzles: an observation from three- to nine-hole nozzles. Exp Therm Fluid Sci Apr. 2019;102:387–96. https://doi.org/10.1016/j.expthermflusci.2018.12.022.

[12] Park J, Choi N, Kim HJ, Park S, Park S. Comparative study on macroscopic and microscopic spray characteristics of surrogate e-gasoline and n-heptane using multi-hole GDI injector. Appl Therm Eng May 2025;266:125584. https://doi.org/10.1016/j.applthermaleng.2025.125584.

[13] Pu T, Wu S, Xie M, Pang Y, Zhang C. Breakup characteristics of ultra-high-pressure GDI spray of a single-hole injector under various thermodynamic conditions. Energy Dec. 2023;285:129413. https://doi.org/10.1016/j.energy.2023.129413.

[14] Huang R, Ni J, Cheng Z, Wang Q, Shi X, Yao X. Assessing the effects of ethanol additive and driving behaviors on fuel economy, particle number, and gaseous emissions of a GDI vehicle under real driving conditions. Fuel Dec. 2021;306:121642. https://doi.org/10.1016/j.fuel.2021.121642.

[15] Shah A, Hoth A, Kolodziej CP, Rockstroh T. Gasoline fuels properties for multi-mode operation – observations in a GDI and the CFR engine. Fuel May 2021;291:119680. https://doi.org/10.1016/j.fuel.2020.119680.

[16] Gainey B, Yan Z, Lawler B. Autoignition characterization of methanol, ethanol, propanol, and butanol over a wide range of operating conditions in LTC/HCCI. Fuel Mar. 2021;287:119495. https://doi.org/10.1016/j.fuel.2020.119495.

[17] Montanaro A, Allocca L, Costa M, Sorge U. Assessment of a 3D CFD model for GDI spray impact against wall through experiments based on different optical techniques. Int J Multiphas Flow Sep. 2016;84:204–16. https://doi.org/10.1016/j.ijmultiphaseflow.2016.05.007.

[18] Taglialatela Scafati F, Pirozzi F, Cannavacciuolo S, Allocca L, Montanaro A. Real time control of GDI fuel injection during ballistic operation mode. Sep. 2015. https://doi.org/10.4271/2015-24-2428.

[19] Lu X, Zhao J, Markov V, Wu T. Study on precise fuel injection under multiple injections of high pressure common rail system based on deep learning. Energy Oct. 2024;307:132784. https://doi.org/10.1016/j.energy.2024.132784.

[20] Payri R, Bracho G, Gimeno J, Bautista A. Rate of injection modelling for gasoline direct injectors. Energy Convers Manag Jun. 2018;166:424–32. https://doi.org/10.1016/j.enconman.2018.04.041.

[21] Oh H, Hwang J, Pickett LM, Han D. Machine-learning based prediction of injection rate and solenoid voltage characteristics in GDI injectors. Fuel Mar. 2022;311:122569. https://doi.org/10.1016/j.fuel.2021.122569.

[22] Yang Z, Stobart R, Winward E. Online adjustment of start of injection and fuel rail pressure based on combustion process parameters of diesel engine. Apr. 2013. https://doi.org/10.4271/2013-01-0315.

[23] Cavicchi A, Postrioti L. Simultaneous needle lift and injection rate measurement for GDI fuel injectors by laser Doppler vibrometry and Zeuch method. Fuel Feb. 2021;285:119021. https://doi.org/10.1016/j.fuel.2020.119021.

[24] Chung N-H, Oh B-G, Sunwoo M-H. Modelling and injection rate estimation of common-rail injectors for direct-injection diesel engines. Proc Inst Mech Eng - Part D J Automob Eng Jun. 2008;222(6):1089–101. https://doi.org/10.1243/09544070JAUTO647.

[25] Ferrari A, Novara C, Vento O, Violante M, Zhang T. A novel fuel injected mass feedback-control for single and multiple injections in direct injection systems for CI engines. Fuel Feb. 2023;334:126670. https://doi.org/10.1016/j.fuel.2022.126670.

[26] Satkoski C, Shaver G. Piezoelectric fuel injection: pulse-to-pulse coupling and flow rate estimation. IEEE ASME Trans Mechatron Aug. 2011;16(4):627–42. https://doi.org/10.1109/TMECH.2010.2048334.

[27] Payri R, Gimeno J, Mata C, Viera A. Rate of injection measurements of a direct-acting piezoelectric injector for different operating temperatures. Energy Convers Manag Dec. 2017;154:387–93. https://doi.org/10.1016/j.enconman.2017.11.029.

[28] Soriano JA, Mata C, Armas O, Ávila C. A zero-dimensional model to simulate injection rate from first generation common rail diesel injectors under thermodynamic diagnosis. Energy Sep. 2018;158:845–58. https://doi.org/10.1016/j.energy.2018.06.054.

[29] Perini F, Busch S, Reitz RD. A phenomenological rate of injection model for predicting fuel injection with application to mixture formation in light-duty diesel engines. Proc Inst Mech Eng - Part D J Automob Eng Jun. 2020;234(7):1826–39. https://doi.org/10.1177/0954407019898062.

[30] Fei H, Liu B, Wang L, Fan L. Optimal estimation of injection rate for high-pressure common rail system using the extended Kalman filter. Measurement Oct. 2023;220:113385. https://doi.org/10.1016/j.measurement.2023.113385.

[31] Wei L, Zhang H, Sun C, Yan F. Simultaneous estimation of ammonia injection rate and state of diesel urea-SCR system based on high gain observer. ISA Trans Jul. 2022;126:679–90. https://doi.org/10.1016/j.isatra.2021.08.002.

[32] Williams Z, et al. Generation of rate-of-injection (ROI) profile for computational fluid dynamics (CFD) model of internal combustion engine (ICE) using machine

learning. Energy and AI May 2022;8:100148. https://doi.org/10.1016/j.egyai.2022.100148.
[33] Choi E, Park J, Hwang J, Oh H, Manin J, Sim HS. Injection rate measurements and Machine-Learning based predictions of ECN Spray A-3 piezoelectric injector. Appl Therm Eng Oct. 2024;254:123827. https://doi.org/10.1016/j.applthermaleng.2024.123827.
[34] Ferrari A, Gurrì S, Vento O. Injected fuel mass and flow rate control in internal combustion engines: a systematic literature review. Energies Dec. 2024;17(24):6455. https://doi.org/10.3390/en17246455.
[35] Ferrari A, Pizzo P, Vento O. Investigation of a GDI injector with an innovative flowmeter for high-pressure transient flows. Int J Engine Res Jul. 2023. https://doi.org/10.1177/14680874231187552.
[36] Ferrari A, Vento O. Thermal effects on Common Rail injection system hydraulic performance. Int J Engine Res Mar. 2023. https://doi.org/10.1177/14680874231162412. 146808742311624.
[37] Ferrari A, Pizzo P, Vento O. Investigation of a GDI injector with an innovative flowmeter for high-pressure transient flows. Int J Engine Res Jul. 2023. https://doi.org/10.1177/14680874231187552.
[38] Toro EF. Riemann solvers and numerical methods for fluid dynamics. Berlin, Heidelberg: Springer Berlin Heidelberg; 2009. https://doi.org/10.1007/b79761.
[39] Ferrari A, Vento O. Influence of frequency-dependent friction modeling on the simulation of transient flows in high-pressure flow pipelines. J Fluid Eng Trans ASME 2020;142(8). https://doi.org/10.1115/1.4046623.
[40] Ferrari A, Zhang T. Benchmark between Bosch and Zeuch method–based flowmeters for the measurement of the fuel injection rate. Int J Engine Res Jan. 2021;22(1):316–27. https://doi.org/10.1177/1468087419827732.
[41] Ferrari A, Paolicelli F. An indirect method for the real-time evaluation of the fuel mass injected in small injections in Common Rail diesel engines. Fuel Mar. 2017;191:322–9. https://doi.org/10.1016/j.fuel.2016.11.053.
[42] Ferrari A, Novara C, Paolucci E, Vento O, Violante M, Zhang T. Design and rapid prototyping of a closed-loop control strategy of the injected mass for the reduction of CO2, combustion noise and pollutant emissions in diesel engines. Appl Energy 2018;232. https://doi.org/10.1016/j.apenergy.2018.09.028.